Title

Performing multi-step chemical reactions in microliter-sized droplets by leveraging a simple passive transport mechanism

Journal

Lab on a Chip, 17(24)

ISSN

1473-0197

Authors

Wang, Jia
Chao, Philip H
Hanet, Sebastian
et al.

Publication Date

2017-12-05

DOI

10.1039/c7lc01009e

Peer reviewed

HHS Public Access

Author manuscript

Lab Chip. Author manuscript; available in PMC 2019 May 22.

Published in final edited form as:

Lab Chip. 2017 December 05; 17(24): 4342–4355. doi:10.1039/c7lc01009e.

Performing multi-step chemical reactions in microliter-sized droplets by leveraging a simple passive transport mechanism

Jia Wang[1,2], **Philip H. Chao**[1,2], **Sebastian Hanet**[1], and **R. Michael van Dam**[1,2,*]

[1]Crump Institute for Molecular Imaging and Department of Molecular & Medical Pharmacology, David Geffen School of Medicine, University of California at Los Angeles (UCLA), Los Angeles, CA, USA

[2]Department of Bioengineering, UCLA, Los Angeles, CA, USA

Abstract

Despite the increasing importance of positron emission tomography (PET) imaging in research and clinical management of disease, access to myriad new radioactive tracers is severely limited due to their short half-lives (which requires daily production) and the high cost and complexity of tracer production. The application of droplet microfluidics based on electrowetting-on-dielectric (EWOD) to the field of radiochemistry can significantly reduce the amount of radiation shielding necessary for safety, and the amount of precursor and other reagents needed for the synthesis. Furthermore, significant improvements in the molar activity of the tracers have been observed. However, widespread use of this technology is currently hinder in part by the high cost of prototype chips and operating complexity. To address these issues, we developed a novel microfluidic device based on patterned wettability for multi-step radiochemical reactions in microliter droplets and implemented automated systems for reagent loading and collection of the crude product after synthesis. In this paper, we describe a simple and inexpensive method for fabricating the chips, and demonstrate the feasibility of prototype chips for performing multi-step radiochemical reactions to produce the PET tracers [^{18}F]fallypride and [^{18}F]FDG, and further show that synthesized [^{18}F]fallypride can be used for *in vivo* mouse imaging.

Keywords

Passive transport; Droplet synthesis; Organic synthesis; Microfluidics; Teflon patterning; Radiochemistry

1 Introduction

Due to the ability to monitor specific *in vivo* biochemical processes with positron emission tomography (PET), this imaging technology is widely used as a research tool in fundamental studies of disease and the development of new drugs and therapies. It is also an indispensable clinical tool for diagnosis and staging of disease, monitoring a patient's response to therapy, and streamlining clinical trials through patient stratification [1–4]. Though

*Corresponding author: mvandam@mednet.ucla.edu.

the majority of scans are performed with the glucose analog 2-[^{18}F]fluoro-2-deoxy-D-glucose ([^{18}F]FDG) to detect abnormal glucose metabolism, there is increasing interest in monitoring other biochemical process using other PET tracers that can provide more disease-specific information in many cases. Though many other tracers are being used in preclinical research and some in clinical trials [5,6], the cost of these tracers compared to [^{18}F]FDG is prohibitive for many studies because there is insufficient demand and coordination of schedules for centralized production and distribution of these short-lived compounds, which is the key to the low cost of [^{18}F]FDG [7]. To increase accessibility to diverse PET tracers, advances are needed in radiosynthesis technology that make it possible to produce smaller batches on demand at an affordable cost.

In recent years there has been significant development of microfluidic devices to perform radiochemical synthesis of PET tracers [8,9]. Among the various approaches that have been explored, droplet-based systems have perhaps the most potential for cost reductions [10,11]. By performing reactions at the microliter scale, amounts of expensive reagents such as precursor can be reduced by 2–3 orders of magnitude compared to conventional approaches. In addition, miniaturization of the overall synthesizer can significantly reduce the cost of equipment and radiation-shielded facilities. Furthermore, the small volume scale reduces contamination, and ^{18}F-labeled tracers can be produced in much higher molar radioactivity due to the reduction of fluorine-19 from reagents and other sources. We have previously shown automated droplet-based radiosynthesis of several PET tracers using electrowetting-on-dielectric (EWOD) systems [12–15]. In EWOD microfluidic chips, electrodes are used to transport reagents, as they are needed, from fixed reagent loading sites to a central, temperature-controlled zone where evaporation and reaction processes are carried out to perform multi-step radiosyntheses. Despite successful implementation, routine use of EWOD for radiochemical synthesis is limited by the complex fabrication of chemically-compatible chips (i.e. based on glass substrates). The large number of processing steps makes the chips expensive and the relatively large surface area (e.g., ~25 mm square) makes it challenging to produce the pinhole-free dielectric layers that are essential to avoid dielectric breakdown and electrolysis of droplets on the chip.

To address these issues, we investigated the use of microfluidic devices relying on passive droplet manipulation to provide the same function of moving reagent droplets from fixed loading sites to a central reaction region. Passive devices do not use electrodes or other active means of actuation, but rather rely on gradients in geometry or surface tension to transport droplets [16]. Xing *et al.* reported a capillary micropumping technique in which droplets could be pumped along superhydrophilic pathways toward a pre-existing larger droplet [17]. Yeh *et al.* reported a method to generate a gradient in the density of hydrophobic decyltrichlorosilane (DTS) molecules on a substrate and observed that droplets moved toward the more hydrophilic side [18]. Similarly, Liu *et al.* reported spontaneous droplet motion on a surface patterned with a gradient in the density of superhydrophilic pillars fabricated within a hydrophobic background [19]. Ng *et al.* reported a method to move droplets using the Marangoni force. An ethanol (EtOH) droplet was positioned next to the water droplet to be actuated. Evaporation of ethanol formed a vapor gradient that dissolved into the surface of the water droplet, and caused the water droplet to move away from the highest ethanol concentration [20]. Droplets can also be made to move spontaneously due to a height

gradient between two non-parallel substrates. Whether the droplet is wetting or non-wetting determines whether it moves toward the side with narrowest or widest height, respectively [21–23]. In another geometric approach, a gradient in the width of a superhydrophilic path on a superhydrophobic surface was reported by Ghosh *et al.* to generate spontaneous motion of a droplet [24]. As seen in Figure 1B, a droplet on such a track experiences an imbalance in surface tension forces along the leading and trailing boundaries of the liquid footprint, leading to a net force on the droplet toward the wider end of the track. Not only is droplet transport possible, but multiple tracks can be merged, or droplets can be held in position until they accumulate enough volume to be further transported.

While these techniques provide a wide range of possible transport mechanisms, not all would be suitable for loading reagents for performing multi-step chemical reactions. For example, capillary pumping relies on the presence of droplets at both the source and destination, but the reaction zone is often completely dried in one or more steps of the synthesis process. In approaches that rely on chemical gradients, the presence of solvents or surface-bound molecules could potentially interfere with, or be affected by, the intended chemical reactions on the chip. Certain geometric gradients (e.g. variation in DTS density on surface or variation in height between two substrates) do not appear to lend themselves to the creation of sophisticated channel networks for multi-step reactions. We therefore elected to work with the approach of Ghosh *et al.*, for which the “channels” can be routed in any direction via simple photolithographic fabrication processes.

We hypothesized that this latter passive transport mechanism could be used to develop a chip for multi-step chemical reactions based on the idea that reagents and solvents are sequentially delivered to a central reaction zone with intervening reaction (heating) and evaporation steps. To pattern the surface, Ghosh *et al.* used a mixture of TiO_2 powder and hydrophobic polymer, and then activated the TiO_2 with UV light in specific regions to catalyze destruction of the polymer [24]. However, TiO_2 has reactive properties [25] that may cause interference with the desired radiochemical reactions, and thus, in this report, we developed an alternative implementation that avoids the use of TiO_2 to generate similar patterned surfaces. In this paper, we discuss the fabrication technique, characterize the movement of several important solvents on patterned surfaces, and design a chip for multi-step reactions. Finally, the multi-step radiosynthesis of two PET tracers, (S)-N-((1-Allyl-2-pyrrrolidinyl)methyl)-5-(3-[^{18}F]fluoropropyl)-2,3-dimethoxybenzamide ([^{18}F]fallypride) and [^{18}F]FDG are demonstrated and then the syntheses are automated by implementation of reagent delivery and product collection mechanisms.

Compared to EWOD microsystems, it is expected that passive microfluidic devices will have advantages of significantly reduced chip cost and enhanced reliability (since the need for a dielectric layer, sensitive to defects, is eliminated entirely). In addition, the overall system should be simpler and less expensive since many droplet operations do not require actively-controlled actuators. Although the idea and mechanism of passive droplet manipulation has been studied for several years, to the best of our knowledge, it has not yet been used as a means to deliver reagents for chemical reactions.

2 Materials and Methods

2.1 Materials

1% Teflon AF 2400 solution was purchased from Chemours. Positive photoresist (MEGAPOSIT SPR 220–7.0) and developer (MEGAPOSIT MF-26A) were purchased from MicroChem (Westborough, USA). Additional solvents and chemicals used for microfluidic chip fabrication, including methanol (MeOH, Cleanroom LP grade), acetone (Cleanroom LP grade), isopropanol (IPA, Cleanroom LP grade), sulfuric acid (96%, Cleanroom MB grade) and hydrogen peroxide (30%, Cleanroom LP grade), were purchased from KMG Chemicals (Fort Worth, USA).

Potassium carbonate (K_2CO_3, 99%), 2,3-dimethyl-2-butanol (thexyl alcohol, 98%), anhydrous hexane (95%), anhydrous ethyl acetate (EtOAc, 99.8%), anhydrous dimethyl sulfoxide (DMSO, 99.9%), methanol (MeOH), EtOH (99.5%), anhydrous acetonitrile (MeCN, 99.8%), ammonium formate (NH_4HCO_2; 97%), 4,7,13,16,21,24-hexaoxa-1,10-diazabicyclo[8.8.8]hexacosane (K222, 98%), trimethylamine (TEA, 99%) and sodium hydroxide (NaOH, 1N) were purchased from Sigma-Aldrich. Tetrabutylammounium bicarbonate ($TBAHCO_3$, 75mM), tosyl fallypride (fallypride precursor, >90%), fallypride (reference standard for [^{18}F]fallypride, >95%) and mannose triflate (FDG precursor, >99%) were purchased from ABX Advanced Biochemical Compounds (Radeberg, Germany). Dulbecco's phosphate-buffered saline (PBS, 1X) was purchased from Mediatech (Manassas, VA, USA). Food dye was purchased from Kroger (Cincinnati, OH, USA) and diluted with deionized (DI) water in the ratio of 1:100 (v/v). DI water was obtained from a Milli-Q water purification system (EMD Millipore Corporation, Berlin, Germany). No-carrier-added [^{18}F]fluoride in [^{18}O]H_2O was obtained from the UCLA Ahmanson Biomedical Cyclotron Facility.

2.2 Design and fabrication of microfluidic droplet reactor

Batches of microfluidic chips were fabricated in the Integrated NanoSystems Cleanrooom (California NanoSystems Institute, UCLA) from 4" silicon wafers using standard lithographic processes. A diagram of the process is shown in Figure S1 of the Supporting Information. The wafer was spin-coated with Teflon AF 2400 solution at 1000 rpm for 30 s and then heated on a hotplate at 160°C for 10 min, 245°C for 10 min, and then annealed in an oven (HTCR 6 28, Carbolite, UK) at 340°C for 3.5 h under nitrogen atmosphere. The final thickness of the Teflon layer was ~150 nm as measured by surface profilometry (Dektak 150, Veeco, Plainview, NY, USA). The Teflon layer was patterned via dry etching [26]. A positive photoresist (SPR 220–7) layer was spin-coated at 3000 rpm for 30 s on top of the Teflon and then soft baked at 115°C for 3 min. After that, the photoresist layer was patterned by UV exposure (MA6 mask aligner, Karl Suss, Garching, Germany) and developed according to the manufacturer's recommended protocol. The exposed Teflon regions were then etched away via 30s exposure to oxygen plasma (PlasmaLab system 80 RIE plus, Oxford Instruments, UK) at 100 mTorr pressure, 200 W power and 50 sccm oxygen flow. The wafer was then diced into individual 25.0 × 27.5 mm microfluidic chips manually with a silicon wafer cutter. Afterwards, chips were dipped into acetone for 1 min to remove photoresist, rinsed in IPA for 1 min, and dried with nitrogen. To further increase

the hydrophilicity of the patterned surface, the microfluidic chips were cleaned with Piranha cleaning solution (96% sulfuric acid; 30% hydrogen peroxide, 3:1 v/v mixture) prior to use. Contact angles of the surface at different steps was measured with a contact-angle goniometer (VCA-3000S, AST, Billerica, MA, USA).

The microfluidic chip comprises a hydrophobic surface with a circular hydrophilic reaction zone in the center (3.0 mm diameter), and six inward-leading tapered hydrophilic pathways for reagent transport (Figure 1A). Liquid reagent droplets are transported passively from reagent loading sites to the central reaction region by the patterned wettability mechanism reported by Ghosh *et al.* [24] (Figure 1B). A simple chip of varied taper angles (α) was also designed to investigate the behavior and droplets of aqueous and organic solvents on the pathway (see Figure S2).

2.3 Automation of microdroplet reactions

Operations on the microfluidic chip were automated by a custom-built temperature control platform, reagent dispensing subsystem and solution collection subsystem.

Heating was provided by placing the chip in direct contact with a ceramic heater (Ultramic CER-1–01-00098, Watlow, St. Louis, MO, USA). The heater was affixed atop a 40 cm x 40 cm thermoelectric device (Peltier, VT-199–1.4–0.8, TE Technology, Traverse City, MI, USA) mounted to a heatsink and cooling fan (AFB0512VHD, Delta Electronics, Taipei, Taiwan). A custom plastic frame above the Peltier (and bolted to the heatsink) helped keep the heater in place while also providing two flat vertical edges for rapidly positioning one corner of the microfluidic chip. The signal from a K-type thermocouple embedded in the heater was amplified through a K-type thermocouple amplifier (AD595CQ, Analog Devices, Norwood, MA, USA) and connected into a data acquisition device (DAQ; NI USB-6211, National Instruments, Austin, TX, USA). A digital output of the DAQ was used to drive a solid-state relay (SSR, Model 120D25, Opto 22, Temecula, CA, USA) to control the supply of 120 VAC to the heater. An on-off temperature controller was programmed in LabView (National Instruments). To cool the heater, the Peltier was driven by a 24V power supply (TDK-Lambda Americas, National City, CA, USA) operated through another SSR controlled by the LabView program. A power step down module (2596 SDC, Model 180057, DROK, Guangzhou, China) was connected to the 24V power supply to provide 12V for the cooling fan, which was switched on during cooling via an electromechanical relay (SRD-05VDC-SL-C, Songle Relay, Yuyao city, Zhejiang, China) controlled by the LabView program.

Droplets were loaded onto the microfluidic chip at reagent loading sites through miniature, solenoid-based, non-contact dispensers (INKX0514300A and INKX0514100A, Lee Company, Westbrook, CT, USA). A different dispenser (INKX0514100A) with seal material made of FFKM was used to dispense the fallypride precursor solution. Other solutions were loaded through dispensers (INKX0514300A) with seal material EPDM. Basically, each dispenser is connected to a pressurized source of a reagent, and the internal solenoid valve is opened momentarily to dispense liquid; the amount of liquid dispensed is related to the duration the valve is open. The inlet of each dispenser was connected to a 1 mL glass V-vial (03–410-024, V Vial™ with Open-Top Screw Cap, Wheaton, Millville, NJ, USA) sealed

with a septum (224100–072, Wheaton) via ETFE tubing (1/16” OD, 0.010” ID, 1529L, IDEX Health & Science, Oak Harbor, WA, USA). The septum was pre-punched with a 1 mm OD biopsy punch (Integra Miltex, York, PA, USA). A bevel was cut on the end of the tubing and positioned at the bottom of the vial. Nitrogen pressure was supplied to the headspace of the vial via a 25G needle (Beckton Dickinson, Franklin Lakes, NJ, USA) inserted directly through the septum. The needle was connected via 1/8” OD tubing to the output of an electronic pressure regulator (ITV0030–3UBL, SMC Corporation, Noblesville, IN, USA) controlled by the LabView program. The reagent stock solutions were pipetted directly into the vial. For precursor solution and [^{18}F]fluoride solution, the smaller volume (30–50 μL) was loaded into a 250 μL vial insert (5181–1270, Agilent Technologies, Santa Clarita, CA, USA) installed into the V-vial. The outlet of each dispenser was fitted with a nozzle (ID 0.005”, INZA4650935K, Lee Company), which is recommended for generation of droplets with volume in the range of 100s of nL to several μL. Each dispenser was powered via a dedicated driver circuit (IECX0501350A, Lee Company) and controlled via the LabView program. Note that because the dispensing rate depends on the driving pressure, viscosity of solvent, tubing size, and nozzle site, a calibration was performed for each type of liquid to determine the valve opening time that should be used to dispense a particular volume (Figure S4). Before use, each dispenser was manually primed (using 3 psi nitrogen) to ensure all air ahead of the liquid was eliminated.

A fixture (Figure 2C) was built to hold 6 dispensers with nozzles ~2 mm above the 6 loading sites of the microfluidic chip. Each dispenser was secured within a hole by an O-ring (ORBN005, Buna-N size 005, Sur-Seal Corporation, Cincinnati, OH, USA). After completing the multi-step reaction, each dispenser was flushed with 1 mL of DI water and MeOH sequentially at 69 kPa (~10 psi), and dried with nitrogen for 2 min.

A liquid collection subsystem was implemented to transfer the final crude reaction product droplet from the microfluidic chip to the collection vial. A 23G hypodermic metal tubing (304H23XX, MicroGroup, Medway, MA, USA) was inserted through a hole in the center of the dispenser fixture. The height of this tube was controlled by mounting it on a single-acting pneumatic cylinder (6498K511, McMaster-Carr, Santa Fe Springs, CA, USA). The pneumatic cylinder was activated by applying 138 kPa (~20 psi) pressure from an electronic pressure regulator (ITV0030–3UBL, SMC Corporation) controlled by the LabView program. In its non-active position, the end of the tubing was ~ 55.5 mm above the chip surface (Figure 2A). The droplet was collected by making close contact (~0.5 mm) to the chip (Figure 2B), and applying vacuum to the headspace of the collection vial using a compact vacuum pump (0–16” Hg vacuum range, D2028, Airpon, Ningbo, China) connected via a vacuum regulator (ITV0090–3UBL, SMC Corporation). Vacuum pressure was ramped from 0 to 21 kPa (~3 psi, 0.01 psi increment every 100 ms) over 30 s to collect the crude product droplet.

After collecting the crude product, the collecting tubing was cleaned by flushing with a 1 mL mixture of MeOH and DI water (1:1, v/v).

2.4 On-chip radiosynthesis

As a demonstration of the ability to perform multi-step reactions with this microfluidic platform, we performed the synthesis of two PET tracers: [^{18}F]Fallypride and [^{18}F]FDG. The synthesis of [^{18}F]Fallypride requires activation of the cyclotron-produced [^{18}F]fluoride via evaporative drying, followed by a fluorination reaction. For [^{18}F]FDG, an initial [^{18}F]fluoride activation step is followed by a fluorination reaction and then a deprotection (hydrolysis) reaction.

2.4.1 Radiosynthesis of [^{18}F]fallypride—The synthesis conditions of [^{18}F]fallypride (Figure 3A) were adapted and further optimized from our previous work synthesizing this compound using EWOD chips [13].

A [^{18}F]fluoride stock solution was prepared by mixing [^{18}F]fluoride/[^{18}O]H_2O (100 μL, ~370 MBq; ~10 mCi) with 75 mM $TBAHCO_3$ solution (5 μL). Precursor stock solution was prepared by dissolving fallypride precursor (4 mg) in a mixture of MeCN and thexyl alcohol (1:1 v/v, 100 μL). A stock solution for dilution of the crude product prior to collection was prepared from a mixture of MeOH and DI water (9:1, v/v, 500 μL). These solutions were loaded into individual reagent vials connected to dispensers.

To perform the on-chip synthesis, a 2 μL droplet of [^{18}F]fluoride solution (~7.4 MBq; ~0.2 mCi) was first loaded onto the chip and spontaneously transported to the reaction site. The microfluidic chip was heated to 105°C for 1 min to evaporate the solvent and leave a dried residue of the [^{18}F]tetrabutylammonium fluoride ([^{18}F]TBAF) complex at the reaction site. It was found that the typical azeotropic distillation process (i.e. addition and evaporation of MeCN) to remove residual moisture was not needed.

Next, a 1 μL droplet of fallypride precursor solution was deposited at another loading site and was spontaneously transported to the reaction site, where it dissolved the dried residue. Then, another 1 μL droplet of fallypride precursor solution was deposited and transported the same way. The chip was heated to 110°C and held for 7 min to accomplish the radiofluorination reaction. Then, ten 1 μL droplets of collection solution were sequentially deposited at a different reagent loading site and spontaneously moved to reaction site to dilute the resulting crude reaction mixture. Afterwards, the diluted droplet was transferred into the collection vial. The collection process was repeated 5x to minimize residue on the chip. A schematic of the on-chip process is shown in Figure 4.

2.4.2 On-chip radiosynthesis of [^{18}F]FDG—The on-chip synthesis conditions for [^{18}F]FDG (Figure 3B) were adapted from the work completed by Gomzina *et al.* [27,28].

A K222/K_2CO_3 stock solution was prepared by dissolving Kryptofix $K_{2.2.2}$ (9 mg) and K_2CO_3 (1.8 mg) in DI water (60 μL). To produce a [^{18}F]fluoride stock solution, 5 μL of this first solution were mixed with [^{18}F]fluoride/[^{18}O]H_2O (45 μL, ~185 MBq; ~5 mCi). A precursor stock solution was prepared by dissolving mannose triflate (2.5 mg) in DMSO (100 μL). For the deprotection step, a NaOH solution (0.3N, 100 μL) was prepared. A stock solution for dilution of the crude product for collection was prepared from a mixture of

MeOH and DI water (3:2 v/v, 500 μL). These solutions were loaded into individual reagent vials connected to dispensers.

For the synthesis, a droplet (2 μL) of [^{18}F]fluoride stock solution (~7.4 MBq; ~0.2 mCi) was first dispensed onto the chip and spontaneously transported to the reaction site. The heater was set to 105°C for 1 min to remove the solvent and leave a dried residue of the [^{18}F]KF/K222 complex. Two droplets of FDG precursor solution (each 1 μL) were sequentially dispensed at another site and moved to the reaction zone. The temperature was raised to 80°C for 5 min to perform the fluorination reaction. Subsequently, a droplet of NaOH solution (3 μL) was dispensed and transported to the reaction site, and the hydrolysis reaction was performed at room temperature for 100 s. Finally, 20 droplets (0.5 μL each) of the collection solution were loaded on the chip sequentially and the resulting diluted crude product was transferred to the collection vial. This collection was repeated four more times.

2.5 Analytical methods

Performance of the chip-based reaction was assessed via measurements of radioactivity and radiochemical purity (RCP).

Radioactivity was measured with a calibrated dose calibrator (CRC-25R, Capintec, Florham Park, NJ, USA) at various times throughout the synthesis process (including starting radioactivity on the chip after loading of [^{18}F]fluoride stock solution). Radioactivity recovery was calculated as the activity of the collected crude product divided by the starting radioactivity, corrected for decay. Collection efficiency was calculated as the activity of the collected crude product divided by the activity on chip after synthesis, corrected for radioactive decay. To gain further insights into the synthesis process, residual activity on the chip was measured after collection of the crude product. We report this as a fraction of the activity on chip just prior to the collection step, corrected for radioactive decay. Similarly, the residual activity in the collection system was measured and expressed as a fraction of the activity on chip just prior to collection, corrected for radioactive decay. In manual syntheses, the residual activity on the pipette tips used for collection was measured in a dose calibrator. In automated syntheses, the residual activity in the collection tubing was determined by measuring the activity of the cleaning solution (1:1 v/v MeOH/water, 1 mL) in a dose calibrator.

RCP of the crude compound collected from the chip was determined via radio thin layer chromatography (radio-TLC). A 1 μL droplet was spotted on a silica TLC plate (JT4449–2, J.T. Baker, Center Valley, PA, USA) with a micropipette. The TLC plate was developed in an appropriate mobile phase and then analyzed with a scanner (MiniGITA star, Raytest, Straubenhardt, Germany).

For [^{18}F]fallypride, the TLC mobile phase was 60% MeCN in 25 mM NH_4HCO_2 with 1% TEA (v/v). In the resulting TLC chromatogram, two peaks are identified: unreacted [^{18}F]fluoride (R_f=0.0) and [^{18}F]Fallypride (R_f=0.9). RCP was calculated as the area under the [^{18}F]fallypride peak divided by the area under both peaks. Fluorination efficiency (conversion of [^{18}F]fluoride to product) was the same as RCP. The decay-corrected crude

radiochemical yield (crude RCY) of [^{18}F]fallypride was defined as the radioactivity recovery times the RCP.

In a few experiments, we also performed radio-HPLC purification of the crude [^{18}F]fallypride mixture and analysis of the purified and formulated [^{18}F]fallypride using a Smartline HPLC system (Knauer, Berlin, Germany) equipped with a degasser (Model 5050), pump (Model 1000), a UV (254nm) detector (Eckert & Ziegler, Berlin, Germany) and a gamma-radiation detector and counter (B-FC- 4100 and BFC-1000; Bioscan, Inc., Poway, CA, USA). Separation was performed using a C18 column (Kinetex, 250 × 4.6 mm, 5 μm, Phenomenex, Torrance, CA, USA). The mobile phase was 60% MeCN in 25 mM NH_4HCO_2 with 1% TEA (v/v) and flow rate was 1.5 mL/min. The retention time of fallypride was 4.5 min. The crude [^{18}F]fallypride mixture collected from the chip was manually injected into the HPLC system, and the [^{18}F]fallypride fraction (~2 mL) was collected. Chromatograms were collected using a GinaStar analog-to-digital converter (raytest USA, Inc., Wilmington, NC, USA) and GinaStar software (raytest USA, Inc.) running on a PC. The chromatogram of crude [^{18}F]fallypride had two peaks, [^{18}F]fluoride (t_R = 1.6 min) and [^{18}F]fallypride (t_R = 4.4 min) (e.g., Figure 5A).

For analysis of only the fluorination reaction of [^{18}F]FDG, the radio-TLC mobile phase was a mixture of MeCN and DI water (95:5, v/v). The resulting chromatogram had two separate peaks, [^{18}F]fluoride (R_f = 0.0) and intermediate [^{18}F]fluoro-1,3,4,6-tetra-O-acetyl-D-glucose ([^{18}F]FTAG, R_f = 0.77). Fluorination efficiency (i.e., conversion of [^{18}F]fluoride to [^{18}F]FTAG) was computed by dividing the area under the [^{18}F]FTAG peak by the sum of the areas of both peaks. For analysis of the [^{18}F]FDG product, two radio-TLCs were performed to enable the efficiency of each reaction (fluorination and hydrolysis) to be inferred [15]. One mobile phase was the same, i.e. a mixture of MeCN and DI water (95:5, v/v). The resulting chromatogram had one distinct peak for [^{18}F]fluoride (R_f = 0.0) and several overlapping peaks corresponding to [^{18}F]FTAG, partially-hydrolyzed [^{18}F]FTAG, and [^{18}F]FDG (R_f > 0) (e.g., Figure 6A). Fluorination efficiency could be calculated from this chromatogram by dividing the sum of the areas under all peaks except [^{18}F]fluoride by the sum of the areas under all peaks. The second mobile phase was a mixture of EtOAc and hexane (1:1, v/v). The first peak (R_f = 0.0) was a combination of unreacted [^{18}F]fluoride and [^{18}F]FDG, while the other overlapping peaks represented a mixture of [^{18}F]FTAG and partially-hydrolyzed [^{18}F]FTAG (e.g., Figure 6B). The RCP of [^{18}F]FDG could be computed as the area under the first peak divided by the area under all peaks, and then subtracting the fraction of unreacted [^{18}F]fluoride (i.e. 1 – fluorination efficiency) from the first radio-TLC chromatogram. The crude RCY of [^{18}F]FDG could be determined by multiplying this RCP by the radioactivity recovery. The hydrolysis efficiency could be determined by dividing the RCP of [^{18}F]FDG by the fluorination efficiency.

[^{18}F]FDG was further purified with a custom miniaturized cartridge[15] adapted from a commercially available FDG Purification cartridge for the base hydrolysis (Chromabond Set V, ABX). The commercial cartridge was designed for macroscale purification of [^{18}F]FDG [29] and would result in too much dilution of the purified product when making small amounts of the tracer. Instead, custom cartridges were made by repacking the resin beads (18.4 mg cation exchange resin ($PS\text{-}H^+$), 18.2 mg anion exchange resin ($PS\text{-}HCO_3$), 30.4 mg neutral

alumina (ALOX N) and 15.6 mg reversed-phase resin (HR-P)) inside a 0.063" ID perfluoroalkoxy alkane (PFA) tubing (ZEUS, Orangeburg, SC, USA). The resins were sandwiched and separated with ~1.5 mm diameter frits (FRPE1CC, OROCHEM, Naperville, IL, USA). Before use, the cartridge was pre-conditioned with 0.5 mL EtOH and then 1 mL DI water. During purification, the ~100 μL diluted crude product was manually passed through the cartridge, then an additional 300 μL DI water were used to collect the pure product. The resulting radio-TLC chromatograms using both mobile phases showed only one [^{18}F]FDG peak. Isolated RCY was calculated by diving the eluted radioactivity ([^{18}F]FDG) by the starting radioactivity ([^{18}F]fluoride). Purification efficiency was calculated as the isolated RCY divided by the crude RCY. After purification, radio-TLC analysis was performed with 95:5 v/v MeCN/H_2O to determine the purity (e.g., Figure 6C). Since the [^{18}F]FTAG and [^{18}F]FDG peaks can partially overlap, radio-TLC analysis using 50:50 v/v EtOAc/hexane was also performed to confirm completion of hydrolysis (e.g., Figure 6D). It should be noted that, due to the small reaction volume, removal of samples for radio-TLC from the crude reaction mixture causes a slight reduction in the total amount of radioactivity. Thus the measurements of isolated product and the estimate of purification efficiency are ~2% lower than they would be if the radio-TLC samples were not taken.

Finally, we also used the technique of Cerenkov imaging [30] to visualize the distribution of radioactivity on the microfluidic chip after different steps. To obtain an image, a glass microscope slide (1mm thick) was placed on top of the chemical reaction chip prior to placing it in the imaging chamber. The Cerenkov imaging setup was described previously [31]. Exposure time was set to 300 s. In addition to performing image corrections (dark mask, flat mask and median mask) described previously, we also performed a background subtraction and a decay correction (to the starting time of the first image). For purposes of analysis, regions of interest (ROIs) were drawn. The background correction used an ROI drawn in an area of the chip not exposed to radioactive solutions; the background level was the average pixel value in this region. Other ROIs analyzed include the total chip, the reaction region, and the reagent pathways. For each experiment trial, images were taken after the evaporation step, the fluorination step and the collection step.

2.6 Micro PET/CT imaging protocol

For *in vivo* imaging, the synthesis was started by preparing a 5x more concentrated [^{18}F]fluoride stock solution consisting of 100 μL [^{18}F]fluoride/[^{18}O]H_2O (i.e. 1850 MBq, 50 mCi) and 5 μL $TBAHCO_3$ solution (75 mM). A 2 μL droplet (~37 MBq; ~1 mCi) was used for the synthesis. The collected (diluted) crude [^{18}F]fallypride product from the chip was purified via analytical-scale HPLC (identical conditions as for analysis described above). The product fraction was dried by evaporation of solvent in an oil bath at 110°C for 8 min with nitrogen flow, and then redissolved in PBS. The amount of PBS was adjusted to ensure 2.6– 3.0 MBq (~70– 80 μCi) of the tracer in 200 μL PBS for one mouse injection. The formulated [^{18}F]fallypride was analyzed via radio-HPLC to confirm purity and determine molar activity according to typical procedures [29]. Isolated RCY was calculated as activity of formulated [^{18}F]fallypride divided by the starting activity.

The *in vivo* imaging study was conducted with a 10 week-old female C57Bl/6J mice (Jackson Laboratory, Bar Harbor, ME) in accordance with UCLA Animal Research Committee approved protocols and guidelines. For static PET imaging, the mouse was pre-warmed, anesthetized (2% isoflurane in oxygen), and injected via tail vein with ~2.6 MBq (~70 μCi) [^{18}F]Fallypride, followed by 60 min uptake period under anesthesia and a 10 min static PET acquisition (G8 PET/CT, Sofie Biosciences, Culver City, CA, USA) with an energy window of 150–650 keV. Images were reconstructed using maximum-likelihood expectation maximization as recommended by the vendor, and corrected for CT-based photon attenuation, detector normalization and radioisotope decay (scatter correction was not applied), and converted to units of percent injected dose per gram (%ID/g). PET scans were followed by a 50 sec CT scan for anatomical co-registration and attenuation correction with a 50 kVp, 200 μA X-ray source and reconstructed using a Feldkamp algorithm. PET/CT images were analyzed using AMIDE version 1.0.5 [32].

3 Results and discussion

3.1 Development of fabrication method

To prepare surfaces with patterned wettability, Ghosh *et al.* [24] deposited a mixture of hydrophobic fluoroacrylic copolymer (PMC), TiO_2 nanoparticles and EtOH onto a substrate, and then used UV irradiation to activate the TiO_2 to catalyze the local destruction of PMC. Because it has been shown the TiO_2 nanoparticles can catalyze a variety of chemical and radiochemical reactions [25], they could therefore potentially interfere with the reactions we wanted to perform on the chip, and thus we avoided the use of nanoparticles. Instead, the patterned surface was prepared by dry-etching of a Teflon coating on a silicon substrate.

Contact angle measurements (Supporting Information, Table S1), made using DI water droplets, showed that the patterned regions (i.e. uncovered silicon surface) were very hydrophilic (θ=7±3°, n=3), while the remaining Teflon regions were very hydrophobic (θ=122±1°, n=3). Importantly, the hydrophobic layer maintained its integrity and adhesion to the substrate throughout the full patterning process.

3.2 Feasibility studies and characterization

First, we assessed whether the passive transport mechanism was compatible with the various solvents and solvent mixtures used in the desired reactions. The simple chip was fabricated to study the behavior of droplets of solvents as a function of taper angle (Supporting Information, Figure S2). We found that all solvents (DI water, MeOH, MeCN, DMSO) could be spontaneously transported for taper angles of 4° or larger (Supporting Information, Figure S3). To provide a safety margin, we used an angle of 5° for subsequent experiments.

We then designed the chemical reaction chip in Figure 1A, consisting of a 3mm diameter hydrophilic reaction zone and six radially-oriented reagent droplet transport ‘channels’. We observed that the droplets behaved differently depending on the type of solvent and the volume. For example, some droplets moved to the central reaction zone and remained confined to this zone, while others would wet the reaction zone and then ‘overflow’ along the radial channels. We suspect that surface tension and density (i.e. gravity) may play a role

in determining this behavior. We empirically explored the behavior of different droplet volumes of each solvent on the 6-inlet chip (Supporting Information, Figure S5) to determine the maximum volume that could be loaded while avoiding the overflow issue. The maximum volumes for DI water, MeOH, MeCN and DMSO were 1, 1, 1, and less than 0.5 μL, respectively. Thus, we adjusted reagent concentrations so the desired absolute amount of reagents could be efficiently loaded without exceeding the maximum droplet volume. To determine a suitable dilution solution for product collection, different combinations of MeOH and DI water were tested after performing mock syntheses. For [^{18}F]fallypride, a ratio of 9:1 (v/v) was used, and for [^{18}F]FDG, a ratio of 6:4 (v/v) was used. These ratios exhibited sufficient mobility to reach the reaction zone, yet avoided overflow of the reaction site (when 1 μL was loaded).

3.3 Mock radiosyntheses

Next, we performed a mock synthesis of [^{18}F]fallypride replacing [^{18}F]fluoride solution with $TBAHCO_3$ solution and precursor solution with just the solvent. Diluted food dyes were added in each solution. A series of photographs of the whole process is shown in Figure 7 (see also the Supplemental Video). Movements of different droplets were fast and smooth. Evaporations proceeded smoothly without bubbling or bursting of droplets. Surprisingly, 2 μL droplets of mock precursor solution remained confined to the reaction site, even though such volume of MeCN caused ‘overflow’, perhaps due to the presence of dried salts ($TBAHCO_3$) and food dye from the evaporation step, or altered the surface properties. The collection process seemed effective, with no visible residue apparent at the reaction site after collection.

The mock synthesis of [^{18}F]FDG was conducted on the chip as well with similar findings. Surprisingly, about 2 μL of the precursor solution could be loaded, even though DMSO volumes >0.5 μL caused overflow.

3.4 Multi-step radiosyntheses

Subsequently, we attempted the radiosyntheses of [^{18}F]fallypride and [^{18}F]FDG. Cerenkov images, showing distribution of radioactivity on the chip at different stages of the syntheses, are shown in Figure 8. Images after the [^{18}F]fluoride drying process showed all the radioactivity confined to the reaction zone, as did images after the fluorination reaction, and images after the collection process showed very little activity remained on the chip. The amount of radioactivity on the whole chip as determined by Cerenkov imaging correlated well with radioactivity measurements made via dose calibrator (data not shown). The [^{18}F]FDG synthesis required some optimization of the [^{18}F]fluoride loading process to ensure radioactivity was well confined (Supporting Information, Figure S6).

Initially, reactions were performed with manual pipetting of reagents to the reagent loading sites and manual collection of the crude product via pipette. Then, fully automated syntheses were performed on the chip, including automated dispensing of reagents and automated collection of the crude product.

The performance of [^{18}F]fallypride synthesis is summarized in Table 1. With manual operations, the fluorination efficiency was 74 ± 8 % (n=4), collection efficiency was 90

± 4 % (n=4), and the crude RCY was 59 ± 9% (n=4). Analysis of radioactivity measurements during the synthesis on passive chips showed negligible losses (−3 ± 1%, n=4, relative to the starting radioactivity) during drying of [^{18}F]fluoride, but slightly higher losses of 15 ± 2% (n=4) during fluorination and 9 ± 4% (n=4) residual activity on chip and pipette tips after collection. Note that the negative evaporation loss is likely due to measurement error in the dose calibrator. The crude RCY was slightly lower than we previously reported for the droplet-based synthesis using EWOD chips, i.e. 84 ± 7% (n=6) [14]. The reported fluorination and collection efficiencies on EWOD were 90 ± 9 % (n=6) and 94 ± 3 % (n=6), respectively, suggesting the current platform and reaction conditions give slightly lower fluorination efficiency. We plan to perform further optimization of conditions and investigation of additional substrate materials in the future. The synthesis time (up to the end of the collection process) for [^{18}F]fallypride was ~25 min.

Automated loading and collection provided a marginal increase in the crude RCY of [^{18}F]fallypride to 64 ± 6 % (n=4). This increase can be explained by the improved radioactivity recovery (84 ± 4 % (n=4) compared to 79 ± 4 % (n=4) for manual operation), which was due to lower residual activity on chip and collection tubing (7 ± 2 % (n=4) of the activity on chip before the collection step, compared to 14 ± 3 % (n=4) for the manual setup). The isolated RCY was 46 ± 4 % (n=4). Typically, in macroscale synthesis, about 5–10% of the radioactivity of the crude product can be lost during purification and formulation. Here we lost about 28% of the activity, suggesting that significant improvements can still be made, perhaps in injection of the small volume of collected product into the HPLC system. The synthesis time was reduced to ~20 min (~12 min for drying and fluorination steps and ~8 min for collection) due to elimination of manual steps. This time is slightly shorter than reported for EWOD-based synthesis (i.e., ~31 min for [^{18}F]fallypride) [14]. The synthesis time is also somewhat shorter than macroscale processes (~29 min for [^{18}F]fallypride) [29,33]. The total time of purification and formulation (~ 13 min) is shorter than macroscale processes as well (20 min) [33]. It should be pointed out that the formulation step was not yet optimized; it is expected that this process could be performed more quickly by using a cartridge based method rather than evaporation. The time for collection can possibly be further condensed by optimizing the speed of the product droplet collection process.

The performance of [^{18}F]FDG synthesis is shown in Table 2. With manual handling, the fluorination efficiency, collection efficiency and crude RCY were 84 ± 4 % (n=4), 70 ± 15 % (n=4) and 40 ± 8 % (n=4), respectively. The intermediate [^{18}F]FTAG was completely hydrolyzed into [^{18}F]FDG as determined by radio-TLC with EtOAc and hexane (1:1, v:v) mobile phase. Evaporation loss (1 ± 2 %, n=4) was minimal, but significant radioactivity losses were observed during fluorination (30 ± 3%, n=4), and there was significant residual radioactivity on the chip and pipette tips after collection (20 ± 9%, n=4). These losses were comparable to the losses reported on EWOD platform (48 ± 3 %, n=2). The crude RCY was marginally lower than crude RCY on EWOD platform (45 ± 10 %, n=2), which was mainly due to lower fluorination efficiency compared to that on EWOD platform (93 ± 3 %, n=2) [14]. The lower fluorination efficiency might due to incomplete dissolution of the [^{18}F]TBAF residue into the precursor droplet. After fluorination, the radioactivity would ideally be uniformly distributed through the reaction droplet, but in fact is confined to a smaller region corresponding to the location of the [^{18}F]TBAF residue after the initial [^{18}F]fluoride drying

step. Further optimizations will focus on improving fluorination efficiency by adding external means to facilitate mixing and dissolution processes, and by carefully controlling volume of solution in reaction site.

As expected, after implementation of automated reagent loading and product collection for [^{18}F]FDG synthesis, the crude RCY was enhanced to 50 ± 8 % (n=4). Higher radioactivity recovery (69 ± 5%, n=4) compared to manual synthesis (49 ± 12 %, n=4) dominated the increase of crude RCY. The collection efficiency for the automated synthesis was 96 ± 2 % (n=4), indicating very little residual activity on the chip or in the collection tubing. (Additional losses of activity occur during the radiofluorination step.) In comparison, for the manual synthesis, the collection efficiency was only 70 ± 15 % (n=4), due primarily to residual activity on the chip (35 ± 16% (n=4) of the activity on the chip prior to the collection step). Isolated RCY was 36 ± 6 % (n=4). Purification efficiency of the custom cartridge was 72 ± 9 % (n=4) and can likely be improved by optimization of the custom purification cartridges and purification process. The synthesis time (up to the end of the collection process) for [^{18}F]FDG was ~21 min, which is much shorter than reported for EWOD-based synthesis (~50 min). The synthesis time including manual purification (11 min) was ~32 min, which is a little bit longer than the macroscale synthesis time (~22 min, including time for purification and sterile filtration) [34]. It should be noted that the purification process was not yet optimized, and it may be possible to reduce the synthesis time further.

3.5 Scaling up the amount of radioactivity

The starting activity of [^{18}F]fallypride and [^{18}F]FDG synthesis was minimized in preliminary experiments for safety reasons to ~7.4 MBq (~0.2 mCi) by loading a 2 μL droplet (radioactivity concentration ~0.1 mCi/μL).

Though sufficient radioactivity was recovered for small animal imaging, it will be desirable in the future to scale this up to enable tracer production for multiple animal studies or for clinical doses. One way to scale up activity is by pre-concentrating the [^{18}F]fluoride solution from the cyclotron using a miniaturized anion exchange cartridges [35]. Another approach is to repeatedly load droplets of [^{18}F]fluoride solution before drying.

Preliminary experiments were conducted to test the feasibility of the latter approach with manual loading and collecting (see Table 3). To ensure the same ratio of precursor to $TBAHCO_3$ in the fluorination reaction, multiple 2 μL droplets of [^{18}F]fluoride/[^{18}O]H_2O solution (i.e. no $TBAHCO_3$) were first loaded, followed by a single 2 μL droplet of $TBAHCO_3$ solution (3.6 mM). The mixture was dried at 105°C for 1 min. In a preliminary experiment, loading of 2, 4, or 8 μL of [^{18}F]fluoride/[^{18}O]H_2O solution resulted in crude RCYs was 58% (n=1), 54% (n=1), and 50% (n=1). This apparent reduction in crude RCY as a function of [^{18}F]fluoride/[^{18}O]H_2O volume could be a mixing issue as it may become increasingly difficult to dissolve the increasing amount of residue in the precursor solution droplet prior to fluorination. Instead of loading a large volume and drying it once, each droplet of [^{18}F]fluoride/[^{18}O]H_2O could be dried after loading, perhaps limiting the lateral extent of the initial residue. For the 8 μL case, the starting activity was 2.34 MBq (~ 0.63 mCi).

3.6 Preclinical Imaging

Using [^{18}F]fallypride synthesized automatically on the chip, *in vivo* small-animal PET/CT imaging was performed after purification (purity > 99%) and reformulation. Separation via radio-HPLC revealed no additional radioactive impurities. Molar activity was 185 GBq/μmol (~5. 0 Ci/μmol) at the end of synthesis. The biodistribution, showing high uptake of [^{18}F]fallylpride in the striatum (Figure 9), was similar to literature reports [36].

4 Conclusions

An automated microfluidic platform for droplet-based reactions was developed based on passive droplet transport using patterned wettability. A new approach to fabricating such patterned surfaces was developed and implemented on silicon substrates. After optimization and characterization were performed to determine optimal taper angle of the pathways and optimal droplet volumes for various solvents, multi-step chemical reactions (including evaporative drying, fluorination and deprotection steps) were performed to synthesize two PET tracers, [^{18}F]fallypride and [^{18}F]FDG. As a demonstration of the ability to produce useful amounts of these tracers, a batch of [^{18}F]fallypride was prepared, purified, formulated, and used for preclinical imaging.

Cerenkov imaging revealed the distribution of radioactivity after various synthesis steps. As desired, the majority of radioactivity was confined in the reaction site during fluoride drying and reaction steps, and minimal residual radioactivity remained on chip after the collection step. More detailed analysis of Cerenkov images may be helpful in further optimization of aspects of the on-chip synthesis such as droplet mixing and redissolution of dried residues.

Though synthesis performance was slightly lower than on EWOD chips, the cost of the passive chips is significantly lower due to the very simple fabrication process. Furthermore, the overall system for connecting reagent sources and collecting the crude product is significantly less complicated. Synthesis times were also shorter than on EWOD chips, potentially enabling the production of more batches of tracers in one day.

By combining with a [^{18}F]fluoride concentrator, or sequentially loading [^{18}F]fluoride droplets, the system can be scaled up to higher amounts of radioactivity. Other than PET imaging, our automated platform has the potential to be applied for small scale chemical reactions or assays as well.

Supplementary Material

Refer to Web version on PubMed Central for supplementary material.

5 Acknowledgments

We thank Dr. Roger Slavik, Dr. Saman Sadeghi, and the staff of the UCLA Biomedical Cyclotron facility for generously providing [^{18}F]fluoride ion for these studies. We also thank Dr. Jason Lee and Charles Zamilpa at the UCLA Crump Institute Preclinical Imaging Technology Center for assistance with preclinical imaging, Jason Jones for assembling ceramic heating and cooling subsystem, Jeffery Collins for providing help with radiochemistry. This work was funded in part by the National Institute on Aging (R21 AG049918), the National Cancer Institute (R21 CA212718, P30 CA016042), the National Institute of Mental Health (R44 MH097271), and the UCLA Foundation from a donation made by Ralph and Marjorie Crump for the UCLA Crump Institute for Molecular Imaging.

6 References

1. Vallabhajosula S, Solnes L and Vallabhajosula B, Semin. Nucl. Med, 2011, 41, 246–264. [PubMed: 21624560]
2. Dunphy MPS and Lewis JS, J. Nucl. Med, 2009, 50, 106S–121S. [PubMed: 19380404]
3. Matthews PM, Rabiner EA, Passchier J and Gunn RN, Br. J. Clin. Pharmacol, 2012, 73, 175–186. [PubMed: 21838787]
4. Piel M, Vernaleken I and Rösch F, J. Med. Chem, 2014, 57, 9232–9258. [PubMed: 25144329]
5. Radiosynthesis Database of PET Probes (RaDaP), http://www.nirs.qst.go.jp/research/division/mic/db2/, (accessed May 8, 2017).
6. Marchand P, Bekaert V, Ouadi A, Laquerriere P, Brasse D and Curien H, J. Nucl. Med, 2013, 54, 15N–17N.
7. Keng PY, Esterby M and van Dam RM, in Positron Emission Tomography - Current Clinical and Research Aspects, ed. Hsieh C-H, InTech, Rijeka, Croatia, 2012, pp. 153–182.
8. Rensch C, Jackson A, Lindner S, Salvamoser R, Samper V, Riese S, Bartenstein P, Wängler C and Wängler B, Molecules, 2013, 18, 7930–7956. [PubMed: 23884128]
9. Pascali G and Matesic L, in Perspectives on Nuclear Medicine for Molecular Diagnosis and Integrated Therapy, eds. Kuge Y, Shiga T and Tamaki N, Springer Japan, 2016, pp. 79–92.
10. Keng PY, Sergeev M and van Dam RM, in Perspectives on Nuclear Medicine for Molecular Diagnosis and Integrated Therapy, eds. Kuge Y, Shiga T and Tamaki N, Springer Japan, 2016, pp. 93–111.
11. Keng PY and van Dam RM, Mol. Imaging, 2015, 14, 579–594.
12. Javed MR, Chen S, Kim H-K, Wei L, Czernin J, "CJ" Kim C-J, van Dam RM and Keng PY, J. Nucl. Med, 2014, 55, 321–328. [PubMed: 24365651]
13. Javed MR, Chen S, Lei J, Collins J, Sergeev M, Kim H-K, Kim C-J, van Dam RM and Keng PY, Chem. Commun, 2014, 50, 1192–1194.
14. Chen S, Javed MR, Kim H-K, Lei J, Lazari M, Shah GJ, van Dam M, Keng PY and Kim C-J, Lab. Chip, 2014, 14, 902–910. [PubMed: 24352530]
15. Keng PY, Chen S, Ding H, Sadeghi S, Shah GJ, Dooraghi A, Phelps ME, Satyamurthy N, Chatziioannou AF, Kim C-J and van Dam RM, Proc. Natl. Acad. Sci, 2012, 109, 690–695. [PubMed: 22210110]
16. Darhuber AA and Troian SM, Annu. Rev. Fluid Mech, 2005, 37, 425–455.
17. Xing S, Harake RS and Pan T, Lab. Chip, 2011, 11, 3642–3648. [PubMed: 21918770]
18. Yeh S-I, Fang W-F, Sheen H-J and Yang J-T, Microfluid. Nanofluidics, 2013, 14, 785–795.
19. Liu C, Sun J, Li J, Xiang C, Che L, Wang Z and Zhou X, Sci. Rep., , DOI:10.1038/s41598-017-07867-5.
20. Ng V-V, Sellier M and Nock V, Int. J. Multiph. Flow, 2016, 82, 27–34.
21. Dangla R, Kayi SC and Baroud CN, Proc. Natl. Acad. Sci, 2013, 110, 853–858. [PubMed: 23284169]
22. Hong J, Park JK, Koo B, Kang KH and Suh YK, Sens. Actuators B Chem., 2013, 188, 637–643.
23. Luo C, Heng X and Xiang M, Langmuir, 2014, 30, 8373–8380. [PubMed: 24979670]
24. Ghosh A, Ganguly R, Schutzius TM and Megaridis CM, Lab Chip, 2014, 14, 1538–1550. [PubMed: 24622962]
25. Sergeev ME, Morgia F, Lazari M, Wang C and van Dam RM, J. Am. Chem. Soc, 2015, 137, 5686–5694. [PubMed: 25860121]
26. Cho C-C, Wallace RM and Files-Sesler LA, J. Electron. Mater, 1994, 23, 827–830.
27. Gomzina NA, Vasil'ev DA and Krasikova RN, Radiochemistry, 2002, 44, 403–409.
28. Koag MC, Kim H-K and Kim AS, Chem. Eng. J, 2014, 258, 62–68.
29. Lazari M, Collins J, Shen B, Farhoud M, Yeh D, Maraglia B, Chin FT, Nathanson DA, Moore M and van Dam RM, J. Nucl. Med. Technol., 2014, 42, 203–210. [PubMed: 25033883]
30. Cho JS, Taschereau R, Olma S, Liu K, Chen Y-C, Shen CK-F, van Dam RM and Chatziioannou AF, Phys. Med. Biol, 2009, 54, 6757–6771. [PubMed: 19847018]

31. Dooraghi AA, Keng PY, Chen S, Javed MR, “CJ” Kim C-J, Chatziioannou AF and van Dam RM, Analyst, 2013, 138, 5654–5664. [PubMed: 23928799]
32. Loening AM and Gambhir SS, Mol. Imaging, 2003, 2, 131–137. [PubMed: 14649056]
33. Lu S, Giamis AM and Pike VW, Curr. Radiopharm, 2009, 2, 1–13.
34. Long JZ, Jacobson MS and Hung JC, J. Nucl. Med. Technol., 2013, 41, 32–34. [PubMed: 23318199]
35. Webster E, Haka M, Zigler S, Patanella J and Young K, J. Nucl. Med, 2015, 56, 1172–1172.
36. Mukherjee J, Constantinescu CC, Hoang AT, Jerjian T, Majji D and Pan M-L, Synapse, 2015, 69, 577–591. [PubMed: 26422464]

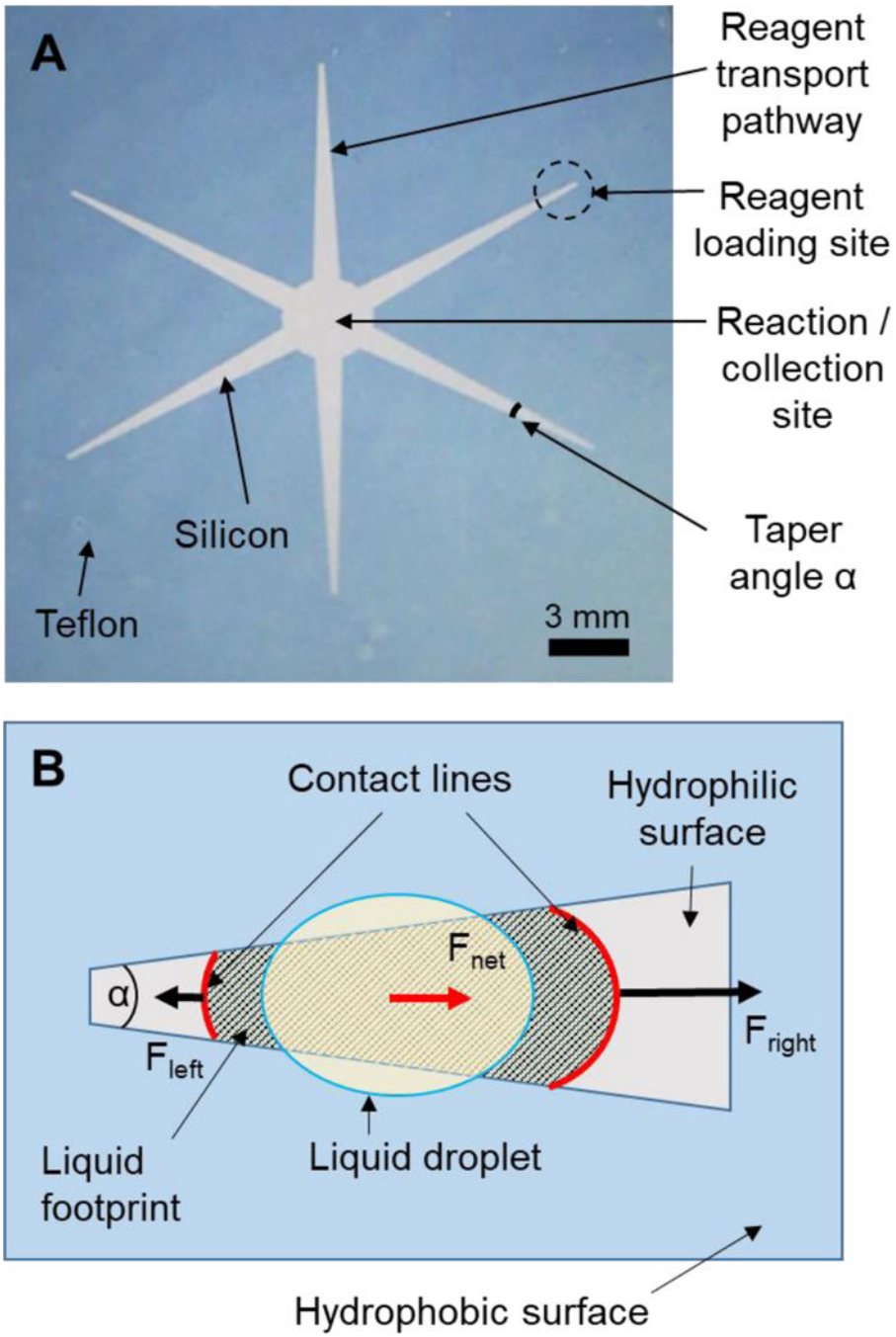

Figure 1.

(A) Photograph of fabricated passive microfluidic chip (top view). The star pattern is a hydrophilic surface (silicon); the remainder is hydrophobic (Teflon). The diameter of the central circular reaction zone is 3.0 mm. The taper angle α of each delivery channel is 5°, and length from the narrow end to center is 9.7 mm. The width of the narrow end of each delivery channel is 0.17 mm. (B) Illustration of passive transport mechanism of a droplet on a wedge-shaped pathway. F_{net} is the net force due to the larger contact line at the leading

(right) edge of the liquid footprint compared to the trailing (left) edge, driving the liquid in the direction of the wider track.

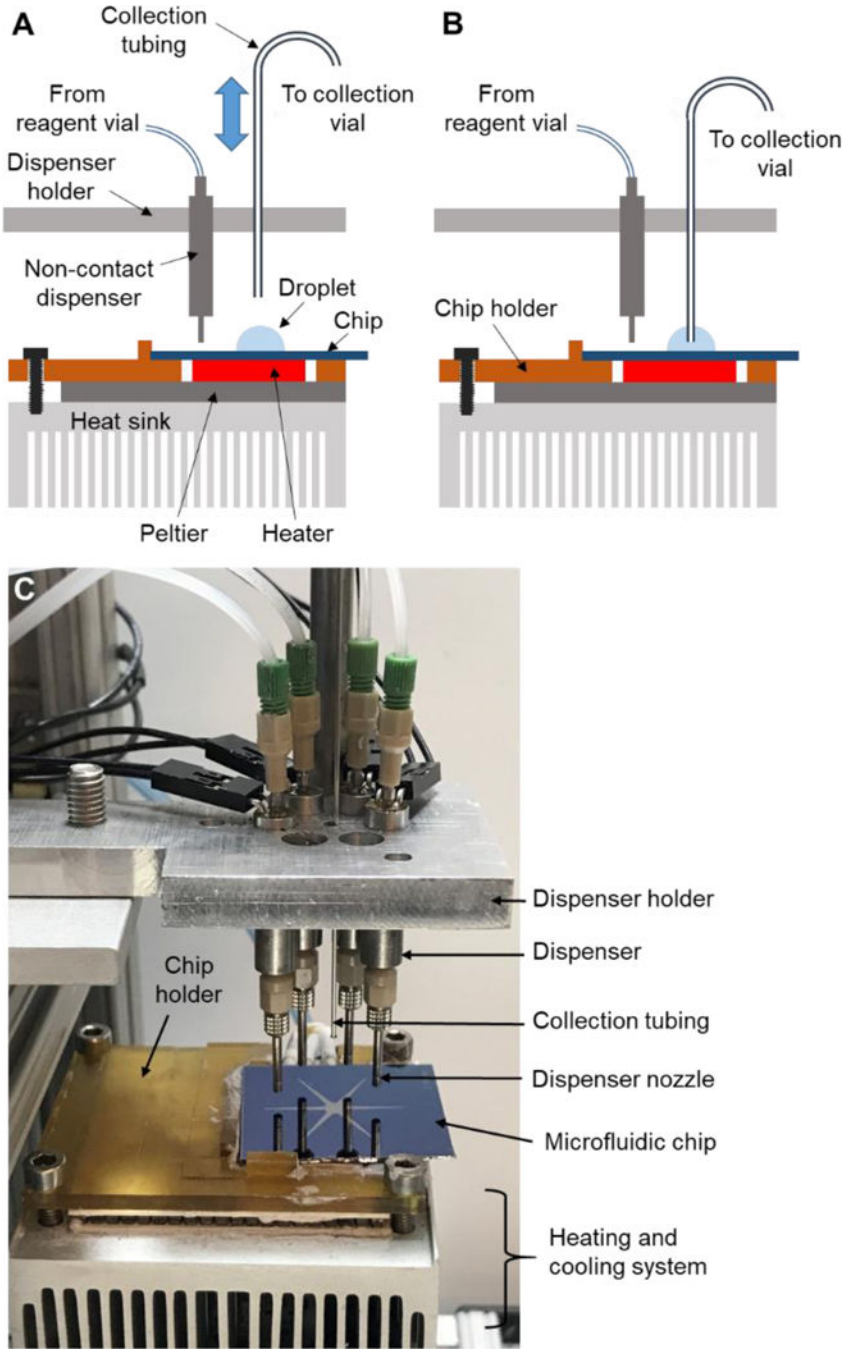

Figure 2.

(A) Schematic of droplet microreactor system, including reagent dispensing system, crude product collection system, and heating and cooling system. (B) Schematic showing configuration for product collection, i.e. with collection tubing lowered into the droplet. The pneumatic cylinder used to lower the tubing is omitted for clarity. (C) Photograph of the microfluidic platform.

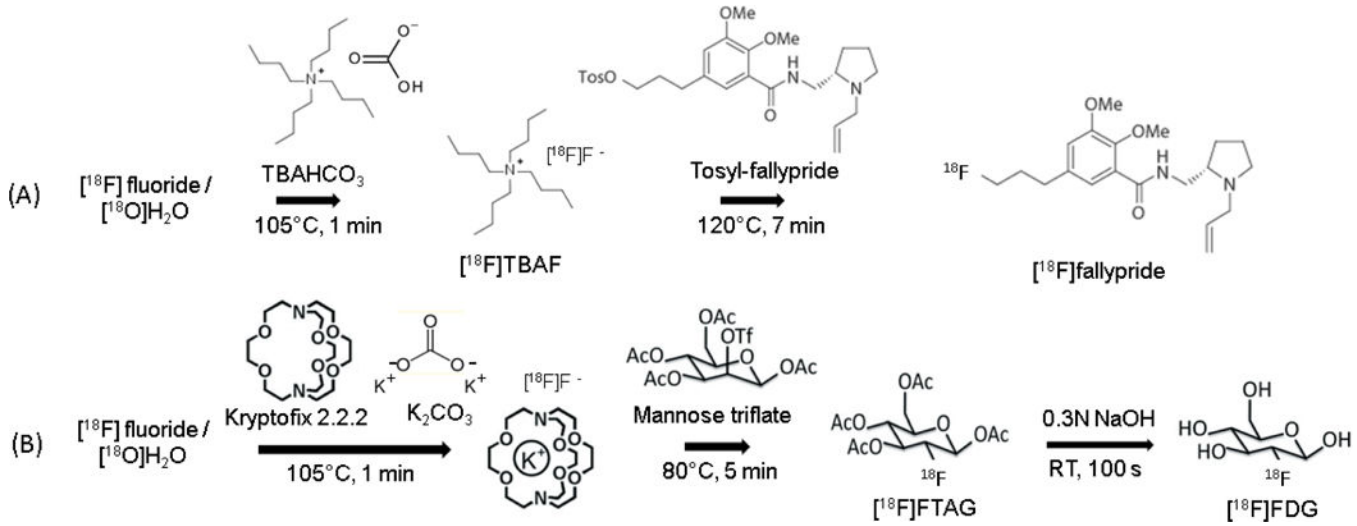

Figure 3.

Synthesis schemes for the example PET radiotracers. (A) Radiosynthesis of [^{18}F]fallypride, illustrating [^{18}F]fluoride drying step followed by radiofluorination of precursor. (B) Radiosynthesis of [^{18}F]FDG, showing the [^{18}F]fluoride drying step, followed by radiofluorination of the precursor and the deprotection (hydrolysis) reaction.

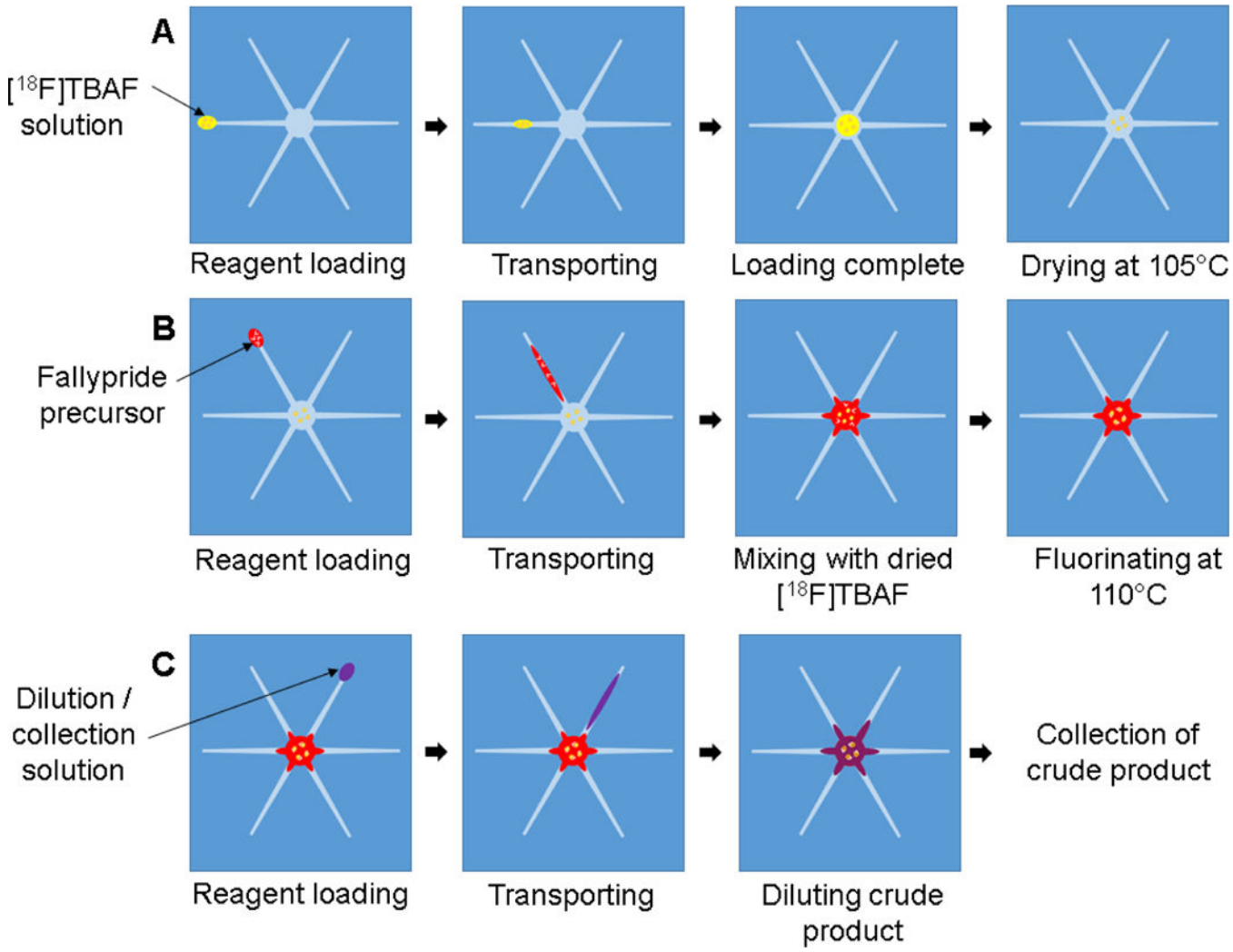

Figure 4.

Schematic of [^{18}F]fallypride synthesis on the passive microfluidic chip. (A) [^{18}F]fluoride solution is loaded and dried. (B) Precursor solution is loaded and fluorination reaction is performed. (C) Collection solution is loaded to dilute the crude product, which is then collected. Note that each reagent is loaded from a dedicated dispenser and reagent pathway. The synthesis of [^{18}F]FDG is quite similar but there is an additional reaction step between steps B and C. After the fluorination reaction, the deprotection agent (NaOH) is added, transported to the center, and the room temperature hydrolysis reaction is performed.

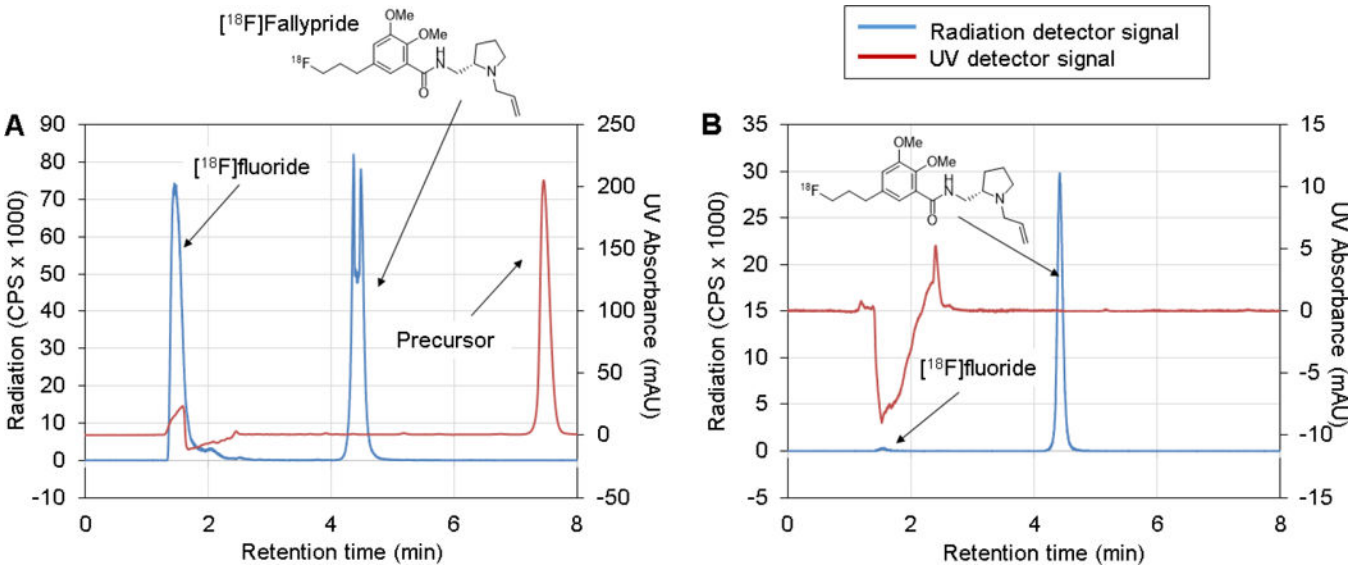

Figure 5.

Examples of radio-HPLC chromatograms of [^{18}F]fallypride synthesis on the microfluidic reaction chip. (A) Analysis of crude product. Note that the apparent double peak of [^{18}F]Fallypride is an artifact due to saturation of the radiation detector. (B) Analysis of formulated product. The RCP was 99%.

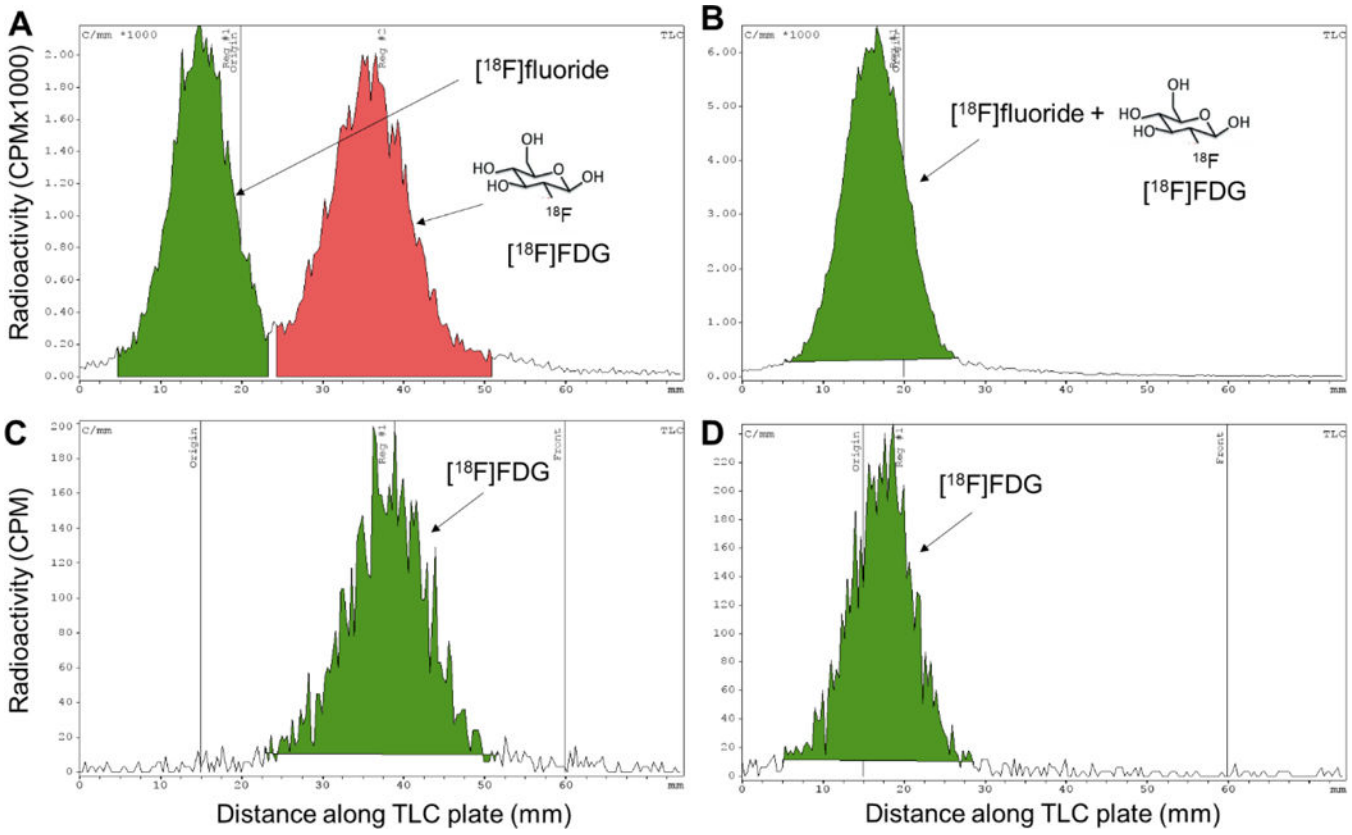

Figure 6.

Examples of radio-TLC chromatograms of [^{18}F]FDG synthesis on the microfluidic reaction chip. (A) Analysis of crude product using 95:5 MeCN/water mobile phase. (B) Analysis of the same sample but using the 50:50 EtOAc/hexane mobile phase. The peak represents both unreacted [^{18}F]fluoride and [^{18}F]FDG, and the absence of a second peak indicates no residual [^{18}F]FTAG or partially hydrolyzed [^{18}F]FTAG. (C) Analysis of purified [^{18}F]FDG using 95:5 MeCN/water mobile phase. The RCP was >99%. (D) Analysis of the same sample, but using the 50:50 EtOAc/hexane mobile phase.

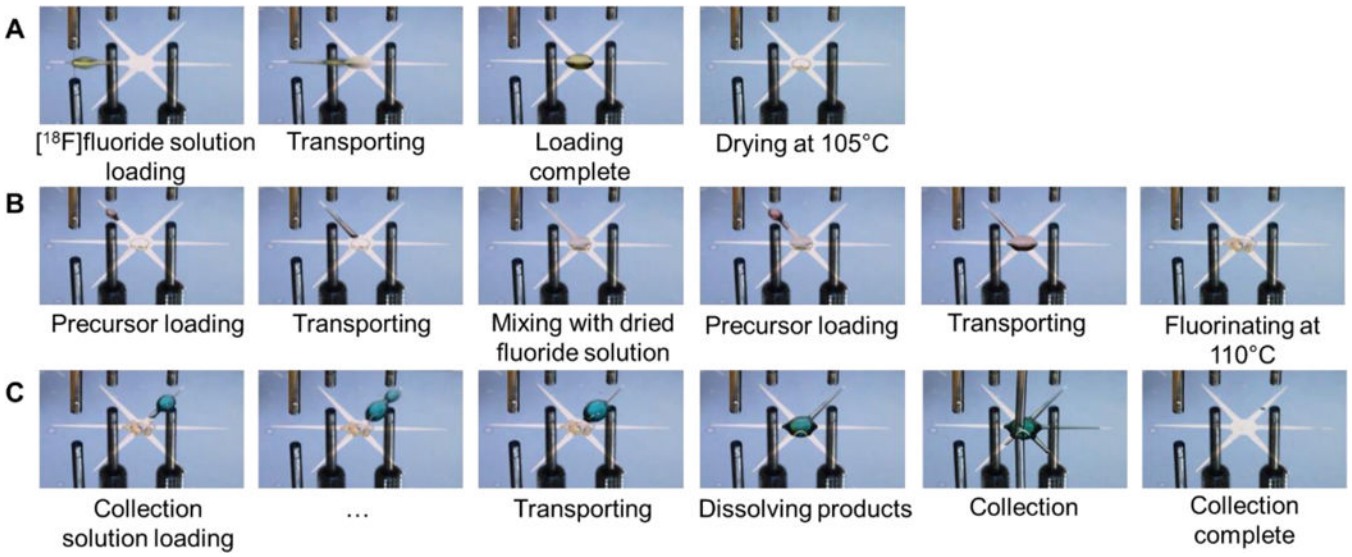

Figure 7.

Sequence of photographs of the microfluidic chip during the mock synthesis of [^{18}F]fallypride. (A) A DI water droplet (2μL, dyed yellow) containing $TBAHCO_3$ (77mM) was loaded, spontaneously transported to the reaction site, and then the chip was heated to 105°C to remove the solvent. (B) Next, two droplets of a 1:1 v/v mixture of MeCN and thexyl alcohol (1μL, dyed red) were loaded from a separate inlet and transported to the reaction site in sequence, after which the droplet was heated to 110°C to simulate fluorination reaction. Note that loading in two separate portions instead of a single larger droplet helped to prevent over-flowing of the reaction site. (C) Next, two droplets of collection solution (9:1 v/v MeOH/water) (5 μL each, dyed blue) were loaded from a third inlet and transported to the center to dilute the reaction mixture. Finally the collection tubing was lowered and the droplet was collected into a vial with the aid of vacuum. Very little residue was apparent on the chip after collection.

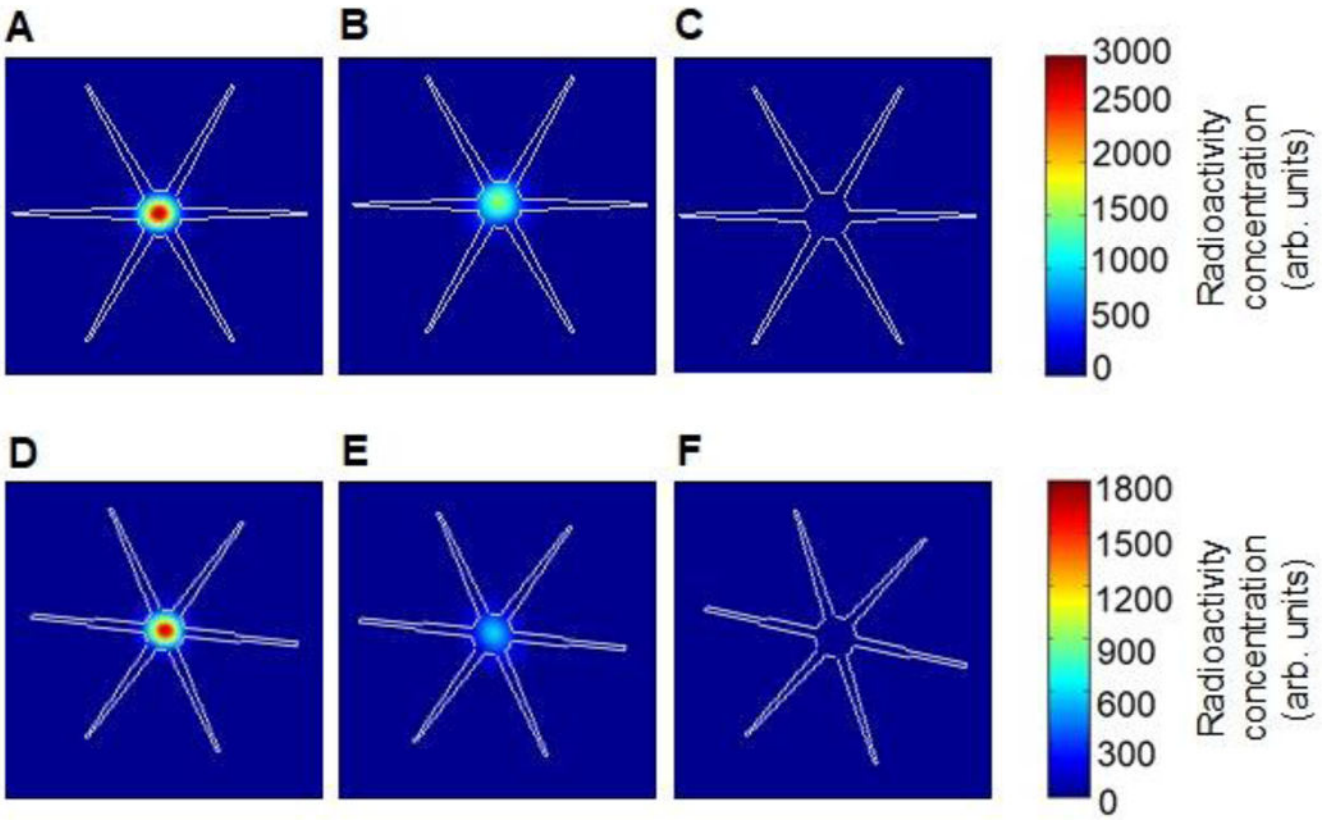

Figure 8.

Distribution of radioactivity visualized using Cerenkov imaging after different steps of radiosyntheses. (Top) [^{18}F]Fallypride: (A) after [^{18}F]fluoride drying step; (B) after fluorination reaction; (C) residual radioactivity on chip after collection of product. (Bottom) [^{18}F]FDG: (D) after [^{18}F]fluoride drying step; (E) after fluorination step; (F) residual radioactivity on chip after collection of product. Images are corrected for radioactive decay.

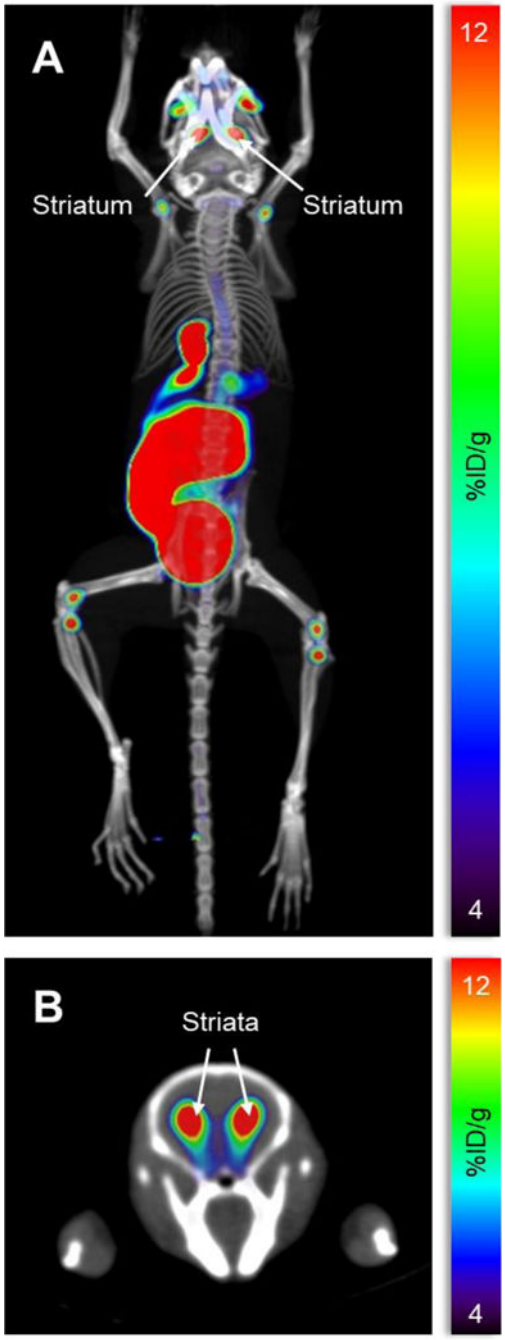

Figure 9.

Small-animal PET/CT images from the static scan after 60 min uptake of [^{18}F]Fallypride. (A) Maximum intensity projection (MIP) image of whole mouse; (B) Transverse slice highlighting uptake in striata in the brain.

Table 1.

Performance of [^{18}F]fallypride synthesis using manual or automated reagent loading and product collection. All measurements were repeated n=4 times. Starting radioactivity was 7.4 MBq (0.2 mCi). Fluorination efficiency, radioactivity recovery, crude RCY, and isolated RCY are expressed with respect to starting [^{18}F]fluoride activity, while collection efficiency and residual activities are expressed with respect to activity on chip just prior to the collection step.

Parameter	Manual synthesis	Automated synthesis
Fluorination efficiency (%)	74 ± 8	76 ± 4
Radioactivity recovery (%)	79 ± 4	84 ± 4
Collection efficiency (%)	90 ± 4	93 ± 2
Synthesis time (min)	25 ± 3	20 ± 1
Crude RCY (%)	59 ± 9	64 ± 6
Isolated RCY (%)	N/A	46 ± 4
Residual activity on chip (%)	12 ± 3	5 ± 2
Residual activity on collection tip/tubing (%)	2 ± 1	2 ± 0

Table 2.

Performance of [^{18}F]FDG synthesis using manual or automated reagent loading and product collection. All measurements were repeated n=4 times. Starting radioactivity was 7.4 MBq (0.2 mCi). Fluorination efficiency, radioactivity recovery, crude RCY, and isolated RCY are expressed with respect to starting [^{18}F]fluoride activity, while collection efficiency and residual activities are expressed with respect to activity on chip just prior to the collection step.

Parameter	Manual synthesis	Automated synthesis
Fluorination efficiency (%)	84 ± 4	72 ± 7
Hydrolysis efficiency (%)	100 ± 0	100 ± 0
Radioactivity recovery (%)	49 ± 12	69 ± 5
Collection efficiency (%)	70 ± 15	96 ± 2
Synthesis time (min)	18 ± 1	21 ± 2
Crude RCY (%)	40 ± 8	50 ± 8
Isolated RCY (%)	N/A	36 ± 6
Residual activity on chip (%)	33 ± 16	4 ± 2
Residual activity on collection tip/tubing (%)	2 ± 0	Not measured

Table 3.

Performance of [^{18}F]fallypride synthesis with scaled-up starting radioactivity. Addition of [^{18}F]fluoride/ [^{18}O]H_2O solutions was followed in all cases by the same amount of $TBAHCO_3$ solution (2 μL, 3.6 mM). All experiments were performed n=1 times.

Parameter	Trial 1	Trial 2	Trial 3	Trial 4
[^{18}F]fluoride/ [^{18}O]H_2O solution volume (μL)	2	4	6	8
Starting radioactivity (MBq)	9	15	21	23
Radioactivity recovery (%)	83	72	76	79
Fluorination efficiency (%)	70	76	57	63
Crude RCY (%)	58	55	43	50